Impact of edge/SOL density fluctuations on ion cyclotron wave propagation and absorption in tokamaks: a stochastic 1D model in a DTT plasma scenario

Vittorio Francalanza[1,2,*], *Alessandro* Cardinali[1,**], *Claudia* Salvia[3], *Giorgio S.* Mauro[1], *Bharat* Mishra[1], *Angelo* Pidatella[1], *Giuseppe* Torrisi[1], *David* Mascali[1,2], and *Roberto* Bilato[4]

[1]Istituto Nazionale di Fisica Nucleare, Laboratori Nazionali del Sud (INFN-LNS), Catania, Italy
[2]Dipartimento di Fisica e Astronomia, Università degli Studi di Catania, Catania, Italy
[3]Centro Ricerche Fusione, Università degli Studi di Padova, Padova, Italy
[4]Max Planck Institute for Plasma Physics, Boltzmannstr. 2, 85748 Garching, Germany

Abstract. This work introduces a novel 1D hybrid modeling approach to investigate how density fluctuations localized in the edge and Scrape-Off Layer (SOL) regions of tokamaks affect ion-cyclotron wave propagation and absorption in a relevant Divertor Tokamak Test (DTT) plasma scenario. The wave-power transmission through the edge is obtained using the Invariant Imbedding Method in the fluctuating layer, while the absorbed power fractions in the smooth core are evaluated with finite-element and Wentzel–Kramers–Brillouin based approaches. Time-independent and spatially correlated density fluctuations are generated analytically via a correlation-matrix method with prescribed root-mean-square amplitude and correlation length, and are superposed on an analytical equilibrium profile. A Monte Carlo approach is then used to sample many realizations and perform statistical analysis. The resulting edge power-transmission distribution exhibits a clearly multi-modal structure, with peaks at high, low, and intermediate transmission levels. The model is fully implemented in Python and is computationally lightweight, making it suitable for fast exploratory studies without the need for high-performance computing resources, which are typical of high-fidelity modeling.

1 Introduction

Ion Cyclotron Resonance Heating (ICRH) is a key technique for plasma heating and current drive in magnetic confinement fusion devices, such as tokamaks. It relies on launching radio-frequency (RF) waves in the tens of MHz range. In ICRH scenarios, the efficiency of wave energy transfer to the plasma strongly depends on the conditions in the edge and Scrape-Off Layer (SOL) regions, where antennas are located. However, these regions are often characterized by steep density gradients and fluctuations, which can substantially modify wave propagation and coupling [1, 2]. Experimental observations in several devices have shown that edge-localized phenomena, such as filamentary structures or Edge Localized Modes (ELMs), can lead to rapid and localized perturbations of the electron density, affecting the accessibility and transmission of the wave into the plasma core [3, 4]. These effects are difficult to capture using traditional full-wave codes, such as TORIC [5], which are typically formulated for static or time-averaged, smooth plasma profiles. Although full-wave tools can achieve short runtimes for given inputs and resolve 2D/3D geometric features (including poloidal variation of perturbations), obtaining statistics over many fluctuating density profile realizations remains computationally demanding. This motivates the development of complementary reduced models that explicitly account for the stochastic nature of the edge/SOL regions and enable efficient Monte Carlo sampling. The aim of this work is to present a novel 1D hybrid strategy to analyze the statistical impact of edge/SOL density fluctuations on ion-cyclotron (IC) wave propagation and absorption. In this paper, the method is demonstrated on a Divertor Tokamak Test (DTT) [6]–relevant plasma scenario, considering one Ion Cyclotron Range of Frequencies (ICRF) configuration and one representative set of fluctuation parameters. Building on previous modeling efforts [7, 8], we analytically introduce spatially correlated density perturbations and analyze their effect on IC wave transmission and absorption using a hybrid numerical scheme that combines the Invariant Imbedding Method (IIM) [9, 10] in the fluctuating plasma layer with finite-element and Wentzel–Kramers–Brillouin (WKB)-based approaches in the smooth plasma core.

2 D(^{3}He) ion heating scenario

The physical configuration adopted in this study refers to a foreseen ICRH minority heating scenario for the DTT facility, where 5% of ^{3}He ions are used as the minority species in a deuterium plasma and the equilibrium density and temperature profiles for electrons, deuterons (D), and minority ^{3}He ions are prescribed using smooth analytical forms consistent with transport modeling (see figure 1). All the geometric and physical parameters adopted

*Corresponding author: francalanza@lns.infn.it
**Corresponding author: cardinali@lns.infn.it

are summarized in table 1, and follow the same configuration used in our previous analyses [7, 8]. We adopt a 2D slab geometry with a Cartesian coordinate system: the normalized radial coordinate is defined as $\hat{x} = r/a'$ with $a' = a + 2.7\,\text{cm}$, so that $\hat{x} = 1$ coincides with the SOL-side sampling location used to extract the antenna electric field (see figure 2), while $\hat{x} = 0$ denotes the plasma center. The toroidal direction, aligned with the equilibrium magnetic field $\vec{B}_0$, is represented by the coordinate z along which a spectral representation of the wave field is introduced with the toroidal refractive index $n_z = c\,k_z/\omega$. The ICRH antenna, operating in the 60–90 MHz range, is modeled as a curved three-strap launcher in COMSOL Multiphysics® [11]. In this study, we fix the operating frequency to 60 MHz. The radiated field component $E_y^{\text{ant}}(z)$ is extracted along a toroidal line at the outboard midplane ($y = 0$) at 2.7 cm from the separatrix, and Fourier-transformed to obtain the antenna spectrum $\tilde{E}_y^{\text{ant}}(n_z)$. The full spectrum is computed on 2^{11} uniformly spaced samples in n_z. It is even in n_z and exhibits two dominant peaks at $n_z = \pm 10$; for $|n_z| > 20$ the magnitude rapidly decays to zero because of the evanescence between the antenna straps and the extraction plane (see figure 3). In this work we employ a reduced discrete sampling that retains the essential pattern of the full spectrum while lowering the computational cost:

$$|n_z| \in \{0, 2, 5, 7, 10, 12, 15, 17, 20\}.$$

Within this framework, we considered only the fast-wave component of the ICRH field and neglect coupling to the slow-wave and Bernstein branches.

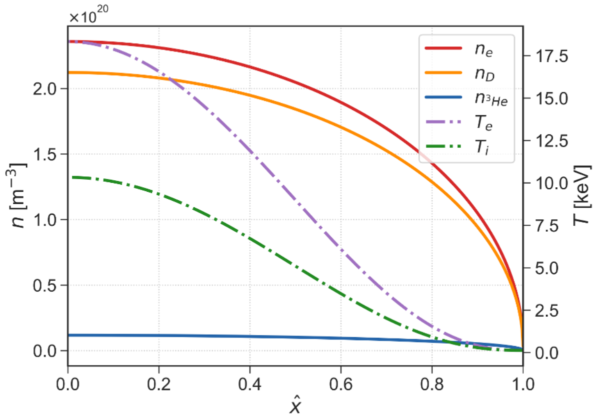

Figure 1. Equilibrium density (solid) and temperature (dash–dotted) profiles vs. $\hat{x}$.

Table 1. Main parameters and profiles for the DTT minority ICRH scenario.

Quantity	Expression / Value
Major radius	$R_0 = 2.19$ m
Minor radius	$a = 0.7$ m
Modified minor radius	$a' = 0.727$ m
Normalized radial coord.	$\hat{x} = x/a'$
Toroidal field on axis	$B_0 = 6.2$ T
Magnetic profile	$B(\hat{x}) = \dfrac{B_0}{1 + a'\hat{x}/R_0}$
ICRH antenna frequency	$f = 60$ MHz

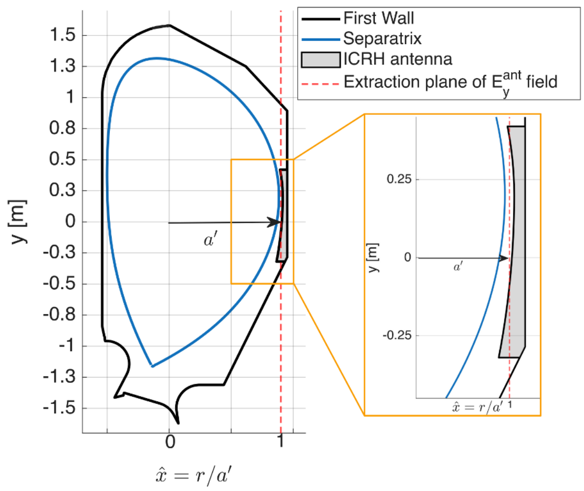

Figure 2. Sketch of a DTT poloidal cross-section with first wall (black), separatrix (blue), and ICRH antenna (grey). The red dashed line at $\hat{x} = 1$ marks where $E_y^{\text{ant}}(z)$ is extracted.

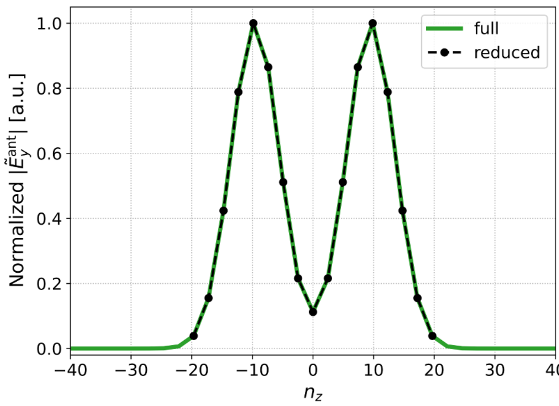

Figure 3. Modulus of the normalized antenna spectrum $|\tilde{E}_y^{\text{ant}}(n_z)|$ vs. n_z: full (solid) and reduced (dash-dotted).

3 Modeling edge density fluctuations

The edge/SOL density fluctuations are modeled as

$$n_e(\hat{x}) = \langle n_e(\hat{x})\rangle + \delta n_e(\hat{x}), \qquad (1)$$

where $\langle n_e(\hat{x})\rangle$ is a smooth equilibrium profile (see figure 1) and $\delta n_e(\hat{x})$ is a zero-mean, spatially correlated stochastic perturbation. Fluctuations are localized to a thin edge/SOL shell, taken here as $0.92 \le \hat{x} \le 1.0$, which corresponds to a radial layer of 6 cm. The purpose of this choice is to demonstrate the current tools, and it can be adapted to more realistic fluctuations. Each realization of $\delta n_e(\hat{x})$ is prescribed by two model input parameters: a relative RMS amplitude (e.g., $\sigma \equiv \delta n/\langle n\rangle = 30\%$) and a spatial correlation length (e.g., $L_c = 1$ cm). These values are illustrative and used here as representative of edge/SOL turbulence; they fall within literature ranges for fluctuation level and correlation length [12], but are not intended as DTT-specific predictions. We define the normalized correlation length as $\hat{L}_c = L_c/a'$. To construct such random fields, we adopt a correlation-matrix approach [13] with the target autocorrelation function defined by:

$$C(\Delta\hat{x}) = \sigma^2 \exp\left(-\frac{|\Delta\hat{x}|}{\hat{L}_c}\right). \tag{2}$$

The correlation matrix $C_{ij} = C(|\hat{x}_i - \hat{x}_j|)$ is then assembled on a discrete radial grid. A Cholesky decomposition $C = LL^T$ allows the generation of spatially correlated fluctuation profiles via:

$$\delta n_e(\hat{x}) = L \cdot \zeta, \tag{3}$$

where ζ is a vector of uncorrelated standard normal random variables, i.e. $\zeta \sim \mathcal{N}(0, 1)$. Figure 4 shows a representative example of a single fluctuating density realization superimposed on the equilibrium background.

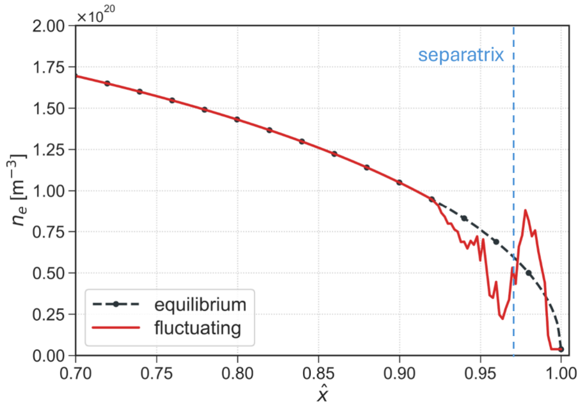

Figure 4. Example of a fluctuating density profile (solid), with $\sigma = 30\%$ and $L_c = 1$ cm, vs. the unperturbed equilibrium profile (dash-dotted).

3.1 Effects on cold-plasma dispersion relation

The cold-plasma dispersion relation for the fast-wave (FW) in a magnetized plasma can be written as:

$$k_x^2(\hat{x}, k_z) = -\left(k_z^2 - \frac{\omega^2}{c^2}S(\hat{x})\right) + \frac{\omega^4}{c^4}\frac{D^2(\hat{x})}{\left(k_z^2 - \frac{\omega^2}{c^2}S(\hat{x})\right)}, \tag{4}$$

where S and D are components of the plasma dielectric tensor that depend on the local density and magnetic field [14]. As $n_e(\hat{x})$ is perturbed by fluctuations, $k_x^2(\hat{x})$ acquires localized spatial modulations. In the smooth case, the profile remains regular, allowing clear identification of propagation and evanescence regions. In contrast, fluctuations introduce sharp radial variations that distort the effective propagation region, potentially generating additional turning points or narrow evanescent barriers. Figure 5 shows a comparison between the dispersion relation in the smooth case and that corresponding to the fluctuating density realization presented in figure 4. The modes $n_z = 10$ and $n_z = 20$ are chosen here as representative of the antenna reduced spectrum (see figure 3). The changes in $k_x^2(\hat{x})$ highlight how edge/SOL perturbations can strongly affect wave evanescence, possibly leading to wave scattering, partial reflections, or local field enhancement depending on the fluctuation geometry.

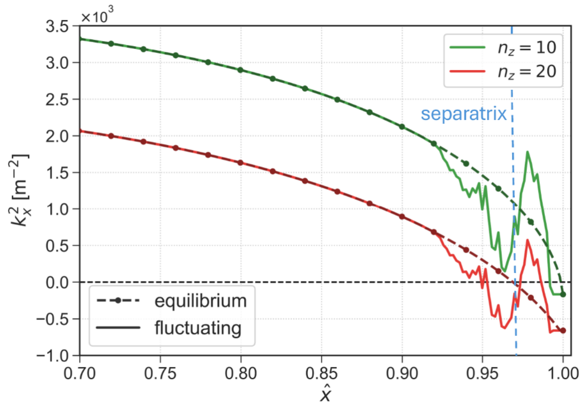

Figure 5. FW cold-plasma dispersion relation for $n_z = 10$ (green) and $n_z = 20$ (red): equilibrium (dash-dotted) vs. the fluctuating (solid) profile corresponding to that of figure 4. The black dashed horizontal line marks $k_x^2 = 0$, locating cutoffs between propagating and evanescent regions.

4 The wave propagation equation

When the coupling with other branches is neglected, the dominant poloidal component of the electric field (E_y) of the fast-wave inside the plasma can be described in our scenario by a one-dimensional, second-order differential equation for the y-component of the field [7, 8], Fourier-transformed in the z direction, $\tilde{E}_y(\hat{x}, k_z)$:

$$\frac{d^2\tilde{E}_y(\hat{x}, k_z)}{d\hat{x}^2} + \hat{\Omega}_c^2(\hat{x}, k_z)\,\tilde{E}_y(\hat{x}, k_z) = 0. \tag{5}$$

The dimensionless complex potential $\hat{\Omega}_c^2$ is defined as:

$$\hat{\Omega}_c^2(\hat{x}, k_z) \equiv k_x^2(\hat{x}, k_z)\,[1 + i\,\gamma(\hat{x}, k_z)]\,a'^2, \tag{6}$$

where $k_x^2(\hat{x}, k_z)$ is the FW cold-plasma dispersion relation and $\gamma(\hat{x}, k_z)$ accounts for wave absorption due to both electrons and ions (see figure 6). The detailed construction of the γ term, including its species decomposition, is reported in [7]. Equation (5) retains the structure of a stationary Schrödinger equation, with $\hat{\Omega}_c^2$ acting as an effective potential that governs the local propagation and damping of the wave. In the fluctuation-free case, the wave equation can be solved via a standard Finite Element Method (FEM) or, equivalently, through a WKB approximation. Boundary conditions are imposed by setting $\tilde{E}_y(\hat{x} = 1, k_z) = \tilde{E}_y^{\rm ant}(k_z)$ at the field extraction point, and by enforcing either a regularity condition at the opposite edge of the domain (assuming the plasma extends to infinity), or by introducing an artificial absorbing layer (Perfectly Matched Layer, PML) at the numerical boundary.

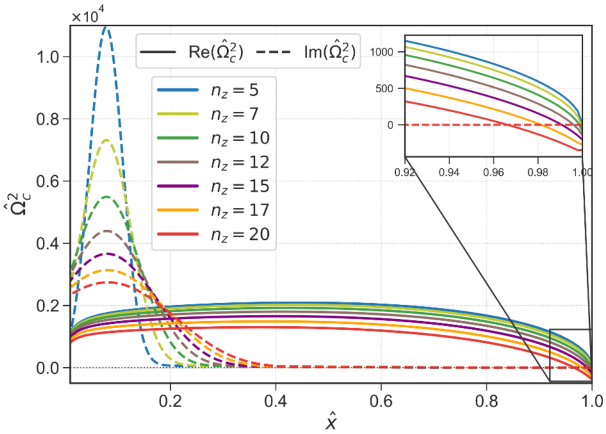

Figure 6. Real (solid) and imaginary (dashed) parts of the dimensionless complex potential $\hat{\Omega}_c^2(\hat{x}, n_z)$ in the fluctuation-free case for a representative set of n_z modes.

4.1 Hybrid IIM-WKB approach for edge/SOL fluctuating plasma

In order to investigate how edge/SOL turbulence affects IC wave transmission and absorption, we implement a novel hybrid numerical method that combines the Invariant Imbedding Method (IIM) in the fluctuating plasma layer with a WKB-like formulation in the fluctuation-free plasma core. The IIM reformulates the boundary-value problem of equation (5) for $\tilde{E}_y(\hat{x}, k_z)$ into an initial-value problem for the total wave reflection and transmission coefficients, without requiring the full-field solution. To this end, we define $\xi \equiv \hat{x}_{\mathrm{start}} - \hat{x}$ as the effective radial thickness of the fluctuating plasma layer, growing from $\xi = 0$ at $\hat{x} = \hat{x}_{\mathrm{start}} \equiv 1.0$ to $\xi = \xi_{\mathrm{edge}}$ at $\hat{x} = \hat{x}_{\mathrm{edge}} \equiv 0.92$ (end of the fluctuating region). As this layer is 'imbedded', the IIM framework tracks the evolution of the complex-valued reflection $R(\xi, k_z)$ and transmission $T(\xi, k_z)$ coefficients, governed by the Bellman-Wing equations [9]:

$$\begin{cases} \dfrac{dR(\xi)}{d\xi} = 2i\,\hat{\Omega}_c(\xi)\,R(\xi) + \dfrac{\hat{\Omega}_c'(\xi)}{2\,\hat{\Omega}_c(\xi)}\,[1 - R^2(\xi)], \\[2ex] \dfrac{dT(\xi)}{d\xi} = i\,\hat{\Omega}_c(\xi)T(\xi) + \dfrac{\hat{\Omega}_c'(\xi)}{2\,\hat{\Omega}_c(\xi)}\,[1 - R(\xi)]\,T(\xi), \end{cases} \tag{7}$$

where $\hat{\Omega}_c' \equiv d\hat{\Omega}_c/d\xi$ and the initial conditions are $R(0, k_z) = 0$ and $T(0, k_z) = 1$. Assuming negligible absorption in the fluctuating layer ($\gamma \simeq 0$), the transmitted power for a given k_z beyond the edge is

$$P^{\mathrm{t}}(k_z) = |T(\xi_{\mathrm{edge}}, k_z)|^2\,P^{\mathrm{ant}}(k_z), \tag{8}$$

with

$$|T(\xi_{\mathrm{edge}}, k_z)|^2 = 1 - |R(\xi_{\mathrm{edge}}, k_z)|^2. \tag{9}$$

and $P^{\mathrm{ant}}(k_z) \propto |\tilde{E}_y^{\mathrm{ant}}(k_z)|^2$. In order to quantify the net coupling through the fluctuating layer, we define the antenna-weighted edge power transmission as the ratio between the total power transmitted at the edge and the total antenna input power:

$$|T_{\mathrm{edge}}|^2 \equiv \frac{\int |T(\xi_{\mathrm{edge}}, k_z)|^2\,P^{\mathrm{ant}}(k_z)\,dk_z}{\int P^{\mathrm{ant}}(k_z)\,dk_z}. \tag{10}$$

To reduce computational cost, we evaluate $|T_{\mathrm{edge}}|^2$ only on the reduced antenna spectrum, i.e. on 17 discrete n_z modes retained from figure 3. Once the power reaching the edge of the core is known, absorption in the smooth, fluctuation-free region ($\hat{x} < \hat{x}_{\mathrm{edge}}$) is computed using a WKB-like approximation. Assuming that the power evolves as $P \propto |E|^2$, we write:

$$P^{\mathrm{abs}}(\hat{x}, k_z) = P^t(k_z)\,\exp\left[-2\delta_0 \int_{\hat{x}_{\mathrm{edge}}}^{\hat{x}} \mathrm{Im}(\hat{\Omega}_c)\,d\hat{x}'\right], \tag{11}$$

$$\frac{dP^{\mathrm{abs}}(\hat{x}, k_z)}{d\hat{x}} = -2\delta_0\,P^t(k_z)\,\mathrm{Im}(\hat{\Omega}_c) \times \exp\left[-2\delta_0 \int_{\hat{x}_{\mathrm{edge}}}^{\hat{x}} \mathrm{Im}(\hat{\Omega}_c)\,d\hat{x}'\right], \tag{12}$$

with $\delta_0 \equiv \omega a'/c$. These expressions allow efficient evaluation of both local and total absorbed power without solving for the electric field in the plasma core. If species-specific absorption is needed, we can set $\gamma = \gamma_s$ to isolate contributions, e.g. γ_e for electrons only or γ_i for ions only. This hybrid method is embedded in a Monte Carlo framework: for each realization of the fluctuating edge/SOL density, the IIM–WKB chain yields the antenna-weighted edge power transmission $|T_{\mathrm{edge}}|^2$, the total absorbed power $P^{\mathrm{abs}}_{\mathrm{tot}}$, and the absorbed-power fractions $P^{\mathrm{abs}}_{\%,\mathrm{e}}$ and $P^{\mathrm{abs}}_{\%,\mathrm{i}}$. The process is then repeated over M Monte Carlo realizations, enabling robust statistical estimates and assessing convergence of the results. We stress that this study employs a single DTT-relevant ICRH minority-heating scenario, one ICRF wave configuration, and one representative set of turbulence parameters, within a reduced 1D slab representation combined with a spectral treatment of the toroidal direction. Poloidal inhomogeneity and full 3D antenna–plasma coupling are therefore explicitly neglected in our model. Accordingly, the method is not intended to deliver quantitatively accurate predictions for DTT, but to provide a fast and computationally efficient framework for exploring the statistical impact of edge/SOL density fluctuations on IC wave propagation and absorption under simplified physics and geometry assumptions.

5 Results

This section presents the main results of the study, based on the FEM approach (for the fluctuation-free case) and the IIM–WKB model (for the edge/SOL fluctuating case).

5.1 Fluctuation-free case.

In the absence of density fluctuations, the full-domain FEM solution is used to reconstruct the electric field

$|E_y(\hat{x}, \hat{z})|$ via the inverse Fourier transform in the normalized toroidal direction $\hat{z} \equiv z/a'$. As shown in figure 7, the field amplitude decreases from the antenna side and drops near the IC absorption region around $\hat{x} \sim 0.2$. Throughout this section the total antenna input power is normalized to $P_{\mathrm{tot}}^{\mathrm{ant}} = 1.0\,\mathrm{MW}$, whereas the expected ICRF power in DTT is $P_{\mathrm{ICRF}} = 6.0\,\mathrm{MW}$. In this fluctuation-free case we obtain an antenna-weighted edge power transmission $|T_{\mathrm{edge}}|^2 = 0.92$ and a total absorbed power $P_{\mathrm{tot}}^{\mathrm{abs}} = 0.92\,\mathrm{MW}$, with the absorbed power partitioned between electrons ($P_{\%,\mathrm{e}}^{\mathrm{abs}} = 33\%$) and ions ($P_{\%,\mathrm{i}}^{\mathrm{abs}} = 67\%$). The corresponding power-deposition profiles are shown in figure 8. These results, especially the contribution of ion absorption, are in good agreement with those obtained using TORIC for the same smooth equilibrium profiles [8].

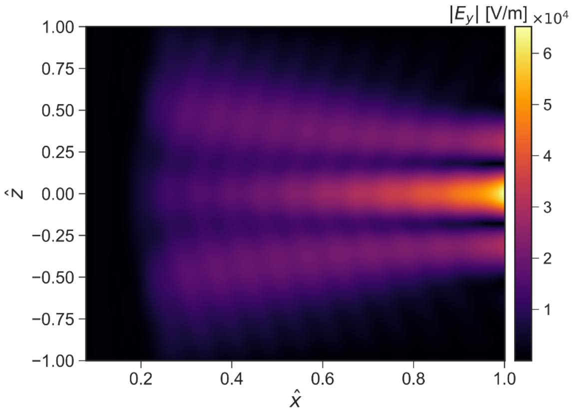

Figure 7. Full-domain FEM solution for $|E_y(\hat{x}, \hat{z})|$.

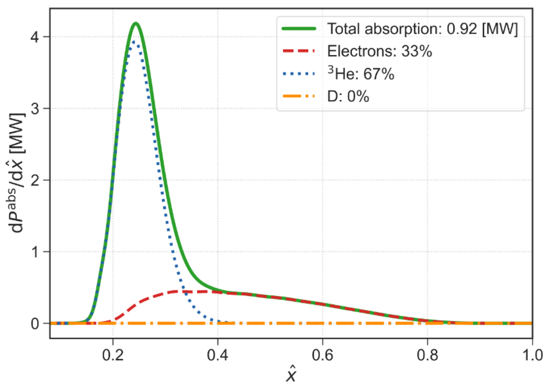

Figure 8. Power deposition profiles expressed as absorbed linear power density $\mathrm{d}P^{\mathrm{abs}}/\mathrm{d}\hat{x}$ vs. $\hat{x}$.

5.2 Edge/SOL fluctuating case

5.2.1 Global statistics

We now focus on the effects of edge/SOL density fluctuations with fixed $\sigma = 30\%$ and $L_c = 1$ cm. For the statistical analysis we performed Monte Carlo (MC) ensembles with up to $M = 5 \times 10^4$ realizations of the fluctuating density, ensuring both the convergence of the statistical estimates and a sufficiently large number of events to obtain well-resolved distributions. Figure 9 shows the normalized histogram of the antenna-weighted edge power transmission $|T_{\mathrm{edge}}|^2$. The distribution is non-Gaussian and clearly exhibits a multimodal behavior: many realizations cluster near $|T_{\mathrm{edge}}|^2 \simeq 1$ (nearly transparent edge/SOL) and a separate group accumulates near $|T_{\mathrm{edge}}|^2 \simeq 0$, with additional secondary modes at intermediate transmission levels. In such a situation, summarizing the ensemble with a single global statistical indicator such as the mean or the median can be misleading. Therefore, to properly describe the results and resolve the different modes explicitly, we partition the sample into four disjoint clusters:

$$\begin{aligned}
\text{A:}\quad & 0.00 < |T_{\mathrm{edge}}|^2 < 0.10,\\
\text{B:}\quad & 0.10 \le |T_{\mathrm{edge}}|^2 < 0.35,\\
\text{C:}\quad & 0.35 \le |T_{\mathrm{edge}}|^2 < 0.70,\\
\text{D:}\quad & 0.70 \le |T_{\mathrm{edge}}|^2 \le 1.00,
\end{aligned}$$

highlighted by the shaded regions in figure 9. In the large MC ensemble used here, clusters A–D account for approximately 23%, 6%, 8%, and 63% of all realizations, respectively. Cluster A comprises the strongly reflecting events, cluster D the nearly transparent ones, while clusters B and C characterize the intermediate-transmission regime.

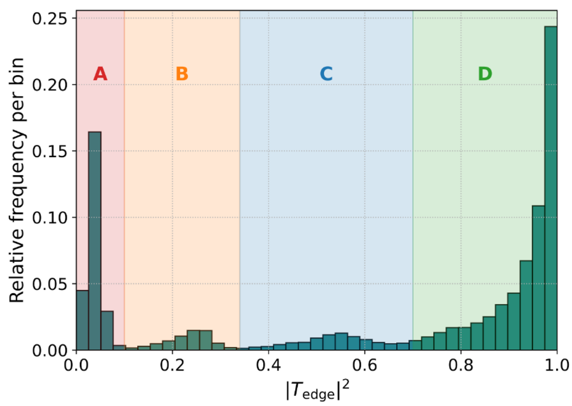

Figure 9. Normalized histogram of the antenna-weighted edge power transmission $|T_{\mathrm{edge}}|^2$ in the reduced-spectrum configuration. Shaded regions define the four clusters A–D used in the statistical analysis.

For each cluster, the distribution of $|T_{\mathrm{edge}}|^2$ obtained from the MC sample is then approximated by fitting a Beta probability density function (PDF) over the corresponding transmission interval. The Beta family is particularly convenient in this context: it can reproduce a wide range of unimodal and skewed shapes with only two parameters, and allows us to use the same functional form for all clusters while keeping the parametrization compact. Figure 10 compares the cluster MC distributions with the fitted Beta PDFs, while fig. 11 shows the associated cumulative distribution functions (CDFs). Each cluster is internally well described by this simple two-parameter PDF family. Table 2 summarizes the statistics for the four transmission

Cluster	$(\alpha_{\rm fit}\,;\,\beta_{\rm fit})$	$\langle \lvert T_{\rm edge}\rvert^2\rangle_{\rm MC}$	$\langle \lvert T_{\rm edge}\rvert^2\rangle_{\rm fit}$	$\Delta_{\rm mean}$ [%]
A	(4.45 ; 7.11)	0.028	0.028	+0.0
B	(2.68 ; 2.25)	0.232	0.230	−0.8
C	(1.89 ; 1.41)	0.530	0.529	−0.2
D	(2.13 ; 0.61)	0.934	0.928	−0.7

Cluster	$\mathrm{Med}(\lvert T_{\rm edge}\rvert^2)_{\rm MC}$	$\mathrm{Med}(\lvert T_{\rm edge}\rvert^2)_{\rm fit}$	$\Delta_{\rm Med}$ [%]
A	0.027	0.028	+3.7
B	0.241	0.232	−3.7
C	0.535	0.534	−0.2
D	0.966	0.951	−1.6

Table 2. MC data statistics and Beta–distribution fits for the four transmission clusters in figure 9. The notation $\langle\cdot\rangle$ and $\mathrm{Med}(\cdot)$ denote respectively the mean and median values. Uncertainties on the MC means are all of the order 10^{-4}.

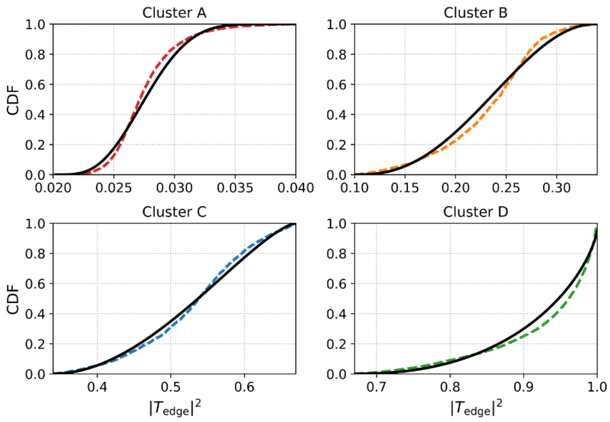

Figure 11. Cumulative distribution functions of $|T_{\rm edge}|^2$ for clusters A–D (dashed lines), compared with the corresponding Beta-fit CDFs (solid lines).

clusters and the corresponding Beta fits. For each cluster we list the mean and the median values of $|T_{\rm edge}|^2$ obtained from the MC sample, together with the values predicted by the fitted Beta distribution and their relative deviations, defined as

$$\Delta_{\rm mean} \equiv \frac{\langle |T_{\rm edge}|^2\rangle_{\rm fit} - \langle |T_{\rm edge}|^2\rangle_{\rm MC}}{\langle |T_{\rm edge}|^2\rangle_{\rm MC}},$$

$$\Delta_{\rm Med} \equiv \frac{\mathrm{Med}(|T_{\rm edge}|^2)_{\rm fit} - \mathrm{Med}(|T_{\rm edge}|^2)_{\rm MC}}{\mathrm{Med}(|T_{\rm edge}|^2)_{\rm MC}}.$$

For all clusters, the deviations between the MC values and the Beta-fit estimates remain below the percentage level for the means and within a few percent for the medians.

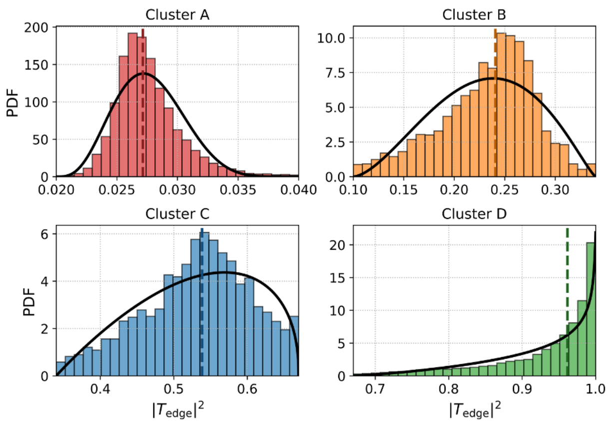

Figure 10. Cluster-wise probability density of $|T_{\rm edge}|^2$ for clusters A–D, together with Beta PDFs fitted on each interval (solid lines). The vertical dashed lines indicate the MC ensemble medians.

5.2.2 *Mode-by-mode contributions to the reduced-spectrum statistics.*

To further investigate how the multimodal structure of the reduced-spectrum transmission distribution arises, we repeat the same MC procedure but restricting the antenna spectrum to new selected subsets of n_z modes. Figure 12 shows the normalized histograms of $|T_{\rm edge}|^2$ obtained from three representative n_z bands: a *low* band $|n_z| \in \{0, 2, 4\}$, an *intermediate* band $|n_z| \in \{5, 7, 10\}$, and a *high* band $|n_z| \in \{12, 17, 20\}$. Each band displays a distinct statistical signature:

- **Low-n_z band.** These modes appear to be less affected by density fluctuations and contribute predominantly to the high-transmission peak ($|T_{\rm edge}|^2 \simeq 1$). They also generate a modest shoulder around $|T_{\rm edge}|^2 \simeq 0.6$, corresponding to realizations in which only a fraction of the low-n_z spectrum propagates through the fluctuating layer.
- **Intermediate band.** This band corresponds with the dominant support of the antenna spectrum and reproduces remarkably well the whole reduced-spectrum transmission distribution, including both main peaks and the small secondary mode around $|T_{\rm edge}|^2 \simeq 0.25$. As a result, this n_z interval captures the essential statistical structure of the reduced case at a substantially lower computational cost (about one third of the runtime of the reduced-spectrum configuration, whose execution time is ~ 300 s).
- **High-n_z band.** These modes show signs of being the most fragile with respect to fluctuations: small changes in the density profile are often sufficient to prevent their access to the core region. As a result, this band contributes predominantly to the low-transmission peak ($|T_{\rm edge}|^2 \simeq 0$), while also generating a weaker shoulder around $|T_{\rm edge}|^2 \simeq 0.5$ associated with realizations in which only a fraction of the high-n_z components is transmitted.

Overall, the multimodal structure of the reduced-spectrum transmission distribution reflects the weighted superposition of several statistically distinct groups of n_z modes. The secondary peaks originate from the contribution of specific n_z bands whose response to the edge/SOL density fluctuations differs markedly from that of the dominant modes.

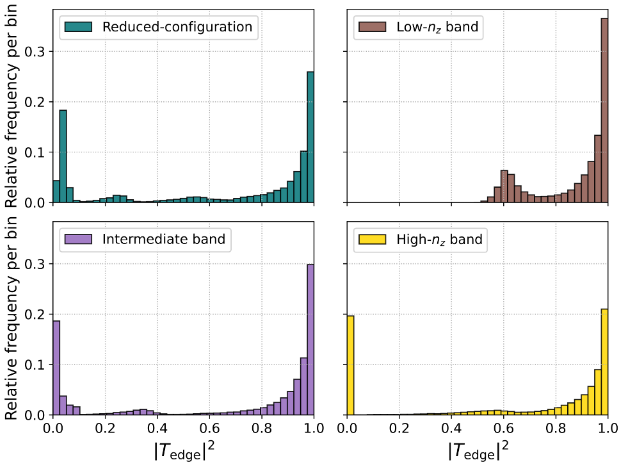

Figure 12. Normalized histograms of $|T_{\text{edge}}|^2$ obtained by restricting the antenna spectrum to selected n_z bands. The intermediate band closely reproduces the main features of the reduced-spectrum configuration $|T_{\text{edge}}|^2$ distribution.

5.2.3 Representative profiles and physical interpretation.

The statistical analyses presented above identify four distinct transmission clusters (section 5.2.1) and show that these arise from the weighted superposition of statistically different n_z sub-populations (section 5.2.2). To better understand the physical origin of these behaviors, we now examine the underlying fluctuation profiles associated with each cluster. For every MC realization we store the fluctuating edge/SOL density profile $n_e(\hat{x})$ and the corresponding FW cold-plasma dispersion relation $k_x^2(\hat{x}, n_z)$, the latter evaluated at $n_z = 10$, where the antenna spectrum is largest and which plays a dominant role in the reduced-spectrum configuration statistics. Within each cluster, we then identify a *medoid* realization, defined as the profile that minimizes the average L^2 distance to all other profiles in the same cluster. This provides a physically realizable and statistically representative fluctuation geometry, in contrast to a simple mean or median profile, which would produce profiles not corresponding to any actual realization. Figure 13 shows the medoid electron–density profiles corresponding to clusters A–D, together with the unperturbed equilibrium background. All medoid profiles coincide with the equilibrium at the inner edge of the fluctuating layer ($\hat{x} = 0.92$), as enforced by the fluctuation model. They begin to diverge noticeably in the outer edge/SOL region and, in particular, close to the field extraction point ($\hat{x} \simeq 1.0$), where the largest density deviations occur. Clusters A, B, and C share a common feature: their edge/SOL densities fall significantly below the equilibrium profile and approach the imposed density floor ($n_{e,\text{floor}} = 3.8 \times 10^{18}$ m^{-3}) near $\hat{x} \simeq 1$. The severity of this depletion decreases progressively from A to C. Cluster A, associated with strongly reflecting events, exhibits the deepest and most extended depletion. Cluster B retains a similar shape but with a milder drop, while cluster C still shows a clear density reduction relative to equilibrium, although less pronounced than in A and B. On the other hand, cluster D behaves qualitatively differently: its medoid profile is systematically above the equilibrium density in the outer edge/SOL region and remains comparatively high all the way to the field extraction point. This overdense behavior, in stark contrast with the depleted profiles of clusters A–C, suggests local plasma conditions that are more favorable to wave propagation through the edge/SOL layer. A further understanding of these trends follows from the analysis of the dispersion relation of the corresponding medoid profiles, as shown in figure 14.

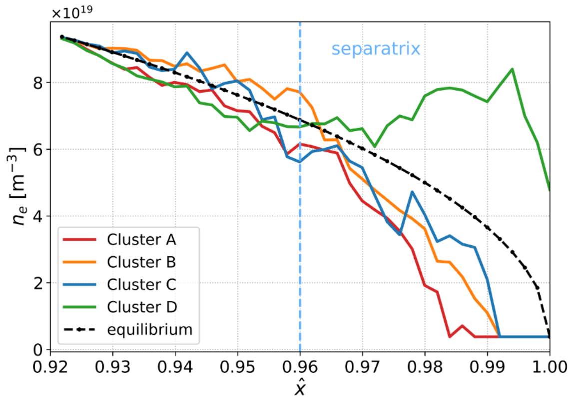

Figure 13. Electron density medoid profiles $n_e(\hat{x})$ in the edge/SOL region for clusters A–D (solid lines), compared with the unperturbed equilibrium profile (black dashed line).

The trends observed in the medoid $n_e(\hat{x})$ profiles are reflected in the behavior of $k_x^2(\hat{x})$. When the edge/SOL density is strongly depleted, as in clusters A and B, the reduction of the cold-plasma coefficients drives k_x^2 below zero over a comparatively wide portion of the outer edge, yielding extended evanescence regions in front of the field extraction point. For cluster C the depletion is milder and the corresponding k_x^2 profile becomes negative only over a shorter and less pronounced layer. These three cases are therefore associated with configurations in which the FW encounters a region where propagation is strongly hampered, consistently with the low (cluster A), intermediate (cluster B) and partial (cluster C) transmission levels found in the statistical analysis. A qualitatively different behavior emerges for cluster D: the overdense edge/SOL profile shifts the cold-plasma response upward and the associated k_x^2 profile stays positive across the entire radial interval, in line with the very high transmission typical of this cluster.

5.2.4 Total absorbed power and species-resolved contributions.

Once the wave reaches the fluctuation-free core, its subsequent evolution is fully determined by the fixed background profiles. Since the damping is sufficiently strong

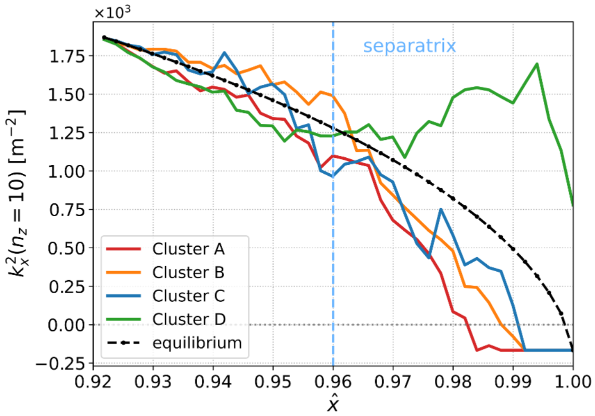

Figure 14. FW cold-plasma dispersion relation $k_x^2(\hat{x}, n_z{=}10)$ for the medoid profiles of clusters A–D (solid lines), compared with the equilibrium profile (black dashed line).

that the power entering the core is almost entirely absorbed before exiting the computational domain, it holds

$$P_{\rm abs}^{\rm tot} \simeq |T_{\rm edge}|^2\, P_{\rm tot}^{\rm ant},$$

so that the statistics of $P_{\rm abs}^{\rm tot}$ closely mirror those of $|T_{\rm edge}|^2$. Regarding the absorbed–power fractions associated with electrons and ions, the analysis performed in the present work does not reveal any significant deviations from the fluctuation-free partition for the considered antenna spectrum. However, a more refined and dedicated investigation—aimed at assessing whether subtle fluctuation-induced effects may emerge under different plasma conditions, fluctuation parameters, or antenna spectra—is left for future work.

6 Summary and conclusions

We presented a novel 1D hybrid modeling framework to investigate how edge/SOL density fluctuations affect IC wave propagation and absorption in a DTT-relevant minority-heating scenario. Fluctuations are generated analytically as time-independent, spatially correlated snapshots via a correlation-matrix method with prescribed RMS amplitude and correlation length, and are sampled in a Monte Carlo ensemble. The IC wave equation is solved with a finite-element method in the fluctuation-free case and, in the fluctuating case, with a hybrid scheme: an Invariant Imbedding Method across the fluctuating layer to obtain the total power transmission, coupled to a WKB treatment in the smooth core for absorbed-power evaluation. Results are reported in terms of the antenna-weighted edge power transmission $|T_{\rm edge}|^2$ and the total and species-resolved absorbed powers. In the fluctuation-free case, results are in good agreement with TORIC calculations performed for the same smooth equilibrium profiles [8], especially for ion absorption. This provides a useful consistency check for the simplified slab geometry and for the hybrid IIM–WKB chain used in the fluctuating case. When edge/SOL density fluctuations are included with fixed $\sigma = 30\%$ and $L_c = 1$ cm, the reduced-spectrum transmission statistics display a pronounced multimodal behavior. The MC ensemble shows a broad spread of $|T_{\rm edge}|^2$ values, with enhanced probability near both nearly transparent events ($|T_{\rm edge}|^2 \simeq 1$) and strongly reflecting events ($|T_{\rm edge}|^2 \simeq 0$), and less frequent secondary modes at intermediate transmission levels. To further investigate the nature of these results we decompose the reduced-spectrum transmission distribution into four clusters, each associated with a distinct transmission range. Also, the role of individual n_z modes is examined by repeating the MC procedure with the antenna spectrum restricted to selected n_z bands. This band-limited analysis reveals that different n_z families carry distinct statistical signatures. To connect these statistical findings to specific plasma features, we classify the fluctuation realizations in each cluster using medoid profiles of the edge/SOL density. The medoid density profiles associated with low- and intermediate-transmission clusters are characterized by progressively less severe edge/SOL depletion, often approaching the imposed density floor in the outermost region. In contrast, the medoid of the high-transmission cluster is systematically overdense with respect to the equilibrium in the outer edge/SOL region. These trends are mirrored in the medoid k_x^2 profiles: depleted edges drive $k_x^2 < 0$ over extended radial intervals, creating broad evanescent regions and thus strong reflection, whereas overdense edges keep $k_x^2 > 0$ across the layer, favoring nearly transparent propagation from the antenna to the core. Taken together, the fluctuation-free benchmark, the cluster-based statistical analysis, the n_z-resolved decomposition and the medoid-profile study all support a single, coherent picture. In the DTT-relevant scenario considered here, edge/SOL density fluctuations act mainly as a near-threshold switch at the edge: by shifting the density profile around the local propagation cutoff, they open or close an effective propagation window for selected n_z bands. Because the antenna spectrum is concentrated in these bands, the system alternates between configurations with almost full reflection and others with nearly complete transparency, while genuinely intermediate transmission levels remain statistically subdominant. While not intended to yield quantitatively precise predictions for DTT, this study provides a new, fast modeling approach that offers approximate guidance on how edge/SOL density fluctuations can condition ICRF coupling, and on which regions of parameter space are most sensitive to edge physics. The toolchain is implemented entirely in Python and requires very modest compute resources (see table 3).

Table 3. Compute resources used for the calculations.

Resource	Value
CPU cores	24 (MC); 4 (FEM)
System RAM	16 GB

7 Future prospects

In future work we plan to: (i) perform parametric scans of fluctuation amplitude, correlation length, and fluctuating-layer thickness; (ii) investigate in detail which fluctuation configurations lead to improved edge transmission, mapping the corresponding parameter regions; (iii) carry out deeper statistical analyses; (iv) extend the study to additional ICRH scenarios, antenna spectra, and tokamaks; (v) benchmark selected cases against COMSOL Multiphysics® and TORIC; and (vi) validate results against published studies and experimental data.

8 Acknowledgment

One of the authors (A.C.) acknowledges support from the Italian National Group for Mathematical Physics (GNFM) of the Istituto Nazionale di Alta Matematica (INdAM). The authors gratefully acknowledge Prof. Renato Spigler for helpful discussions about the "Invariant Imbedding Method" for the solution of the wave equation. The authors also thank the referee for the insightful comments, which helped improve the clarity of this paper.

References

[1] N. Bonanomi et al., Edge turbulent transport toward the L–H transition in ASDEX Upgrade and JET-ILW, Phys. Plasmas **28**, 052504 (2021). https://doi.org/10.1063/5.0040247

[2] J.H. Zhang, W. Zhang, X.J. Zhang, C.M. Qin, Y.Q. Yang and L. Shi, Influences of plasma density perturbations on ion cyclotron resonance heating, Nucl. Fusion **63**, 046012 (2023). https://doi.org/10.1088/1741-4326/acb607

[3] D.N. Hill, A Review of ELMs in Divertor Tokamaks, J. Nucl. Mater. **241-243**, 182 (1997). https://doi.org/10.1016/S0022-3115(97)80039-6

[4] B. Kurzan, H.D. Murmann, J. Neuhauser, and the ASDEX Upgrade Team, Fine structure of type-I edge localized modes in the steep gradient region in ASDEX Upgrade, Rev. Sci. Instrum. **76**, 073504 (2005). https://doi.org/10.1063/1.1935010

[5] M. Brambilla, Numerical simulation of ion cyclotron waves in tokamak plasmas, Plasma Phys. Control. Fusion **41**, 1 (1999). https://doi.org/10.1088/0741-3335/41/1/001

[6] F. Romanelli et al., Divertor Tokamak Test facility project: status of design and implementation, Nucl. Fusion **64**, 112015 (2024). https://doi.org/10.1088/1741-4326/ad5740

[7] C. Salvia et al., Semi-analytical model of ion cyclotron resonance heating antenna-plasma coupling and wave propagation in hot magnetized plasma, Plasma Phys. Control. Fusion **67**, 045001 (2025). https://doi.org/10.1088/1361-6587/adc506

[8] A. Cardinali et al., ICRH modeling of DTT in full power and reduced-field plasma scenarios by full wave codes, Plasma Phys. Control. Fusion **67**, 085018 (2025). https://doi.org/10.1088/1361-6587/adf774

[9] R. Bellman and G.M. Wing, An Introduction to Invariant Imbedding, Classics in Applied Mathematics, Vol. 8, SIAM, Philadelphia (1992). Reprint of the 1975 Wiley edition. https://doi.org/10.1137/1.9781611971279

[10] G.I. Babkin and V.I. Klyatskin, Invariant Imbedding Method for Wave Problems, Wave Motion **4**, 195 (1982). https://doi.org/10.1016/0165-2125(82)90026-7

[11] S. Ceccuzzi et al., Progress in the development of the ICRF system of DTT, Fusion Eng. Des. **213**, 114849 (2025). https://doi.org/10.1016/j.fusengdes.2025.114849

[12] S.J. Zweben et al., Edge turbulence measurements in toroidal fusion devices, Plasma Phys. Control. Fusion **49**, S1 (2007). https://doi.org/10.1088/0741-3335/49/7/S01

[13] W.H. Press et al., Numerical Recipes: The Art of Scientific Computing, 3rd ed. (Cambridge University Press, 2007).

[14] T.H. Stix, Waves in Plasmas, (Springer Science & Business Media, 1992).